Journal of
Composites Science

MDPI

Article

Establishing Benchmark Properties for 3D-Printed Concrete: A Study of Printability, Strength, and Durability

Alise Sapata [1], Māris Šinka [1,*], Genādijs Šahmenko [2], Lidija Korat Bensa [3], Lucija Hanžič [3], Katarina Šter [3], Sandris Ručevskis [4], Diāna Bajāre [2] and Freek P. Bos [5]

1 3D Concrete Printing Laboratory, Institute of Sustainable Building Materials and Engineering Systems, Riga Technical University, 1 Paula Valdena Street, LV-1048 Riga, Latvia; alise.sapata@rtu.lv
2 Institute of Sustainable Building Materials and Engineering Systems, Riga Technical University, LV-1048 Riga, Latvia; genadijs.sahmenko@rtu.lv (G.Š.); diana.bajare@rtu.lv (D.B.)
3 The Department of Materials, Slovenian National Building and Civil Engineering Institute, SI-1000 Ljubljana, Slovenia; lidija.korat@zag.si (L.K.B.); lucija.hanzic@zag.si (L.H.); katarina.ster@zag.si (K.Š.)
4 Institute of High-Performance Materials and Structures, Riga Technical University, Kipsalas Iela 6A, LV-1048 Riga, Latvia; sandris.rucevskis@rtu.lv
5 School of Engineering and Design, Technical University of Munich, 80333 Munich, Germany; freek.bos@tum.de
* Correspondence: maris.sinka@rtu.lv

Abstract: This study investigates the fresh state and hardened state mechanical and durability properties of 3D-printed concrete. The mechanical tests focused on its anisotropic behavior in response to different load orientations. Compressive, flexural, and splitting tensile strengths were evaluated relative to the print layers orientation. Results showed that compressive strength varied significantly, achieving 85% of cast sample strength when the load was applied parallel to the print layers ([u] direction), 71% when the load was applied perpendicular to the print object's side plane ([v] direction), while only reaching 59% when applied perpendicular to the top plane ([w] direction). Similar trends were observed for flexural strength, with average values reaching 75% of cast sample strength when the load was applied perpendicular to the print layers ([v.u] and [w.u] directions), but decreasing to 53% when the load was applied parallel to print layers ([u.w] direction), underscoring the weaknesses at interlayer interfaces. The splitting tensile strength remained relatively consistent across print orientations, reaching 90% of the cast sample strength. Durability assessment tests revealed that 3D-printed concrete exhibits reduced resistance to environmental factors, particularly at the layer interfaces where the cold joint was formed, which are prone to moisture penetration and crack formation. These findings contribute valuable insights into the mechanical and durability properties of 3D-printed concrete, emphasizing the importance of print orientation and interlayer bonding in its performance. This understanding helps guide the optimal use of 3D-printed elements in real-life applications by aligning load or exposure to environmental factors with the material's strength and durability characteristics.

Keywords: additive manufacturing; 3D printing; concrete; cement-based mortar; durability; mechanical properties; fresh state properties

check for updates

Academic Editors: G. Beulah Gnana Ananthi and Krishanu Roy

Received: 4 December 2024
Revised: 14 January 2025
Accepted: 23 January 2025
Published: 7 February 2025

Citation: Sapata, A.; Šinka, M.; Šahmenko, G.; Korat Bensa, L.; Hanžič, L.; Šter, K.; Ručevskis, S.; Bajāre, D.; Bos, F.P. Establishing Benchmark Properties for 3D-Printed Concrete: A Study of Printability, Strength, and Durability. *J. Compos. Sci.* **2025**, *9*, 74. https://doi.org/10.3390/jcs9020074

Copyright: © 2025 by the authors. Licensee MDPI, Basel, Switzerland. This article is an open access article distributed under the terms and conditions of the Creative Commons Attribution (CC BY) license (https://creativecommons.org/licenses/by/4.0/).

1. Introduction

The mechanical properties of 3D-printed concrete are significantly influenced by its layer-by-layer construction, resulting in anisotropic properties [1] and weaker interlayer bonds compared to conventional concrete [2]. Understanding how mechanical properties

vary with the loading direction is crucial, as this directly affects the practical application and safety of 3D-printed concrete in construction [3].

One of the main challenges associated with additive manufacturing technology, particularly in extrusion-based concrete printing, is the inadequate interlayer adhesion between concrete filaments, resulting in weak bonds between consecutively extruded layers. This issue leads to low interlayer bond strength, negatively affecting both mechanical properties and durability [4,5].

Multiple mechanisms contribute to weak interlayer bonding in 3D-printed concrete; however, the main consideration is the loss of surface moisture after extrusion [6]. After extrusion, water evaporates from the exposed concrete surface, leaving it drier than the next layer extruded on top of it. Right after the top layer is extruded, the bottom layer starts absorbing moisture from the top one. As the water is mitigating from bottom to top, air is being forced out from the bottom layer. This air moves to the interlayer region, making it more porous and permeable. Additionally, the lost water due to evaporation leads to additional amounts of unhydrated cement in the interlayer zones [5,7]. Longer time gaps between layer placements further weaken interlayer bonding [5,8].

Anisotropic properties arise not only from weak interlayer regions but also from the anisotropic nature of the filaments themselves. As a result of the extrusion forces, material is compacted more in the print direction, resulting in differing mechanical characteristics [9].

Concrete is typically known for its strong durability as a building material. How-ever, studies show that 3D-printed concrete elements show decreased durability properties when compared to conventionally cast elements. This can mostly be attributed to the pore structure and interconnectivity in printed versus conventionally cast elements.

By using X-ray micro-computed tomography (μCT), it has been shown in the literature that the voids in printed elements are more elongated and interconnected, unlike the large, round, and distinct voids observed in conventionally cast samples [5,10]. The elongated and connected pore structure is especially evident in the interlayer regions [11]. As a result of this, permeability of 3D-printed structures is increased, which contributes to increased water absorption and carbonation rates.

Uneven shrinkage can occur in freshly deposited concrete layers as they cool and dry, leading to reduced durability. This is caused by microcracks that develop due to the restraint from the underlying layer, especially when there is a longer time interval between layer deposits [12,13].

Various studies have shown that longer time intervals between layer deposits weaken compressive strength and interlayer bonding due to reduced surface moisture and an increased number of voids [14–16]. Consequently, it is crucial to minimize conditions that allow water to evaporate. However, in practical applications, there are cases where cold joints are inevitable due to technological constraints and other factors. Cold joints occur when a new layer is applied to one that has already begun to set, creating a weak interface that compromises structural integrity. Therefore, this study has investigated the impact of cold joints on durability.

However, the main objective of this study is to assess the mechanical and durability properties using the specific concrete mixture and printing process described in this study. Variations in these properties in different orientations were studied for two main reasons: first, to use this mixture as a benchmark in further research developing other similar concrete mixtures suited for 3D printing; second, understanding how these properties vary in different directions informs how to best use printed structures in different applications. This helps identify the most suitable uses for the material, critical directions to avoid under load, and optimization of the design for better performance.

The study uses a series of experimental methods to evaluate mechanical strength and durability in different orientations. The specific experimental methods selected are based on study plans created for interlaboratory studies of mechanical properties [17] and durability [18] of hardened concrete and fresh properties of 3D-printed concrete. These guidelines were developed by two technical committees of RILEM (International Union of Laboratories and Experts in Construction Materials, Systems and Structures)—304-ADC, Assessment of Additively Manufactured Concrete Materials and Structures; and 303-PFC, Performance Requirements and Testing of Fresh Printable Cement-Based Materials—with a goal to establish international standards for accuracy and reliability.

Mechanical property testing, such as tensile, compressive, and flexural tests, were conducted along various directions to identify directional strength differences. Durability was assessed through environmental exposure tests—water absorption and carbonation. Additionally, this study examined how interlayer regions and cold joints affect these properties.

2. Materials and Methods

This section outlines the materials and methods employed to evaluate the fresh properties, mechanical performance, and durability of the 3D-printed and -cast specimens. Detailed descriptions of the testing procedures, materials, and equipment used are presented in the following chapter.

2.1. Materials

A commercially available Sakret Ltd. (Rumbula, Latvia) concrete ready mix for 3D printing was used in this test (Table 1). The dry mixture consisted of ordinary Portland cement (OPC) CEM I 42.5 R from Schwenk Ltd. (Broceni, Latvia), limestone filler (Saulkalne, Latvia), sand from Sakret Ltd. (Rumbula, Latvia) with a particle size ranging from 0 to 2 mm, superplasticizer (SP), a viscosity modifying agent (VMA), and polypropylene fiber in the amount of 0.05 wt% with a diameter of 22 µm and length of 6 mm.

Table 1. Used dry mixture in g of 1 kg of dry mixture.

CEM I/A-LL 42.5, Schwenk	Limestone Filler, Saulkalne	Sand, fr. 0–2 mm, Sakret	Additives	Polypropylene Fiber
300	200	490	10	0.5

Various admixtures were already incorporated into the used concrete ready mix to improve the characteristics of 3D-printed concrete during different stages of the printing process.

Superplasticizer was added to decrease the yield stress and plastic viscosity of the concrete by dispersing the binder particles [3,19,20]. In this mixture, melamine sulphonate was used as an SP to reduce water content for optimal extrusion and therefore improve mechanical properties.

When designing a concrete mixture for 3D printing, SPs and VMAs are often used in combination with each other. Most VMAs are able to adsorb simultaneously on several cement particles and bridge them, promoting particle flocculation [20]. For concrete additive manufacturing, the main advantage of adding VMA to the mixture is its ability to increase the yield stress of cementitious materials and reduce material deformation under its own weight, which is vital for achieving high buildability. VMAs can also help prevent segregation in highly flowable concretes and improve water retention. In this mixture, cellulose was added as a VMA due to its compatibility with melamine-based SP [19,21].

Another additive used to improve the shape stability of a structure was polypropylene fibers. Although the addition of these fibers increases the viscosity during mixing and

pumping, they improve the homogeneity and stability of the mix when the material is at rest after extrusion [20,22]. The addition of fibers also improves the flexural strength and reduces cracking from drying shrinkage.

The commercially available concrete ready mix was chosen for its easy accessibility and its potential to provide a controlled and reproducible reference point and benchmark in future studies after evaluating its mechanical and durability properties. Unlike laboratory-made mixtures, a commercially produced mix offers the advantage of minimizing variability in properties that can occur when using different batches or suppliers of individual dry ingredients or when substituting ingredients that may not always be available. This ensures greater uniformity and reliability for comparison when exploring custom admixtures or variations in mix designs.

2.2. Mixing and 3D Printing

Mixtures for mechanical, durability, and fresh-state tests were prepared in three different batches of 45, 30, and 15 L volume, respectively. Each batch was prepared following the same procedure by first mixing the dry ingredients with water for 180 s, then allowing the mixture to rest for 10 min, and then remixing for an additional 60 s with a mixing speed of 680 rpm. The prepared mix was then manually loaded into the hopper.

The printing system features a gantry-type printer (Figure 1) controlled by a computer and has three degrees of freedom. The allowed printing area is 1000 × 1000 × 1500 mm. In this study, a round nozzle with a diameter of 36 mm was used to achieve the desired filament width. Based on the prior experience of laboratory workers and visual observations during printing, including dimensional consistency, layer compaction, interlayer adhesion, and absence of surface tearing, the printing speed was set to 6950 mm/min to ensure optimal print quality.

(**a**) (**b**)

Figure 1. Custom-made laboratory concrete printer at RTU: (**a**) printer setup with the aluminum frame and print area; (**b**) gantry system closeup: (1) motor; (2) hopper; (3) inlet; (4) pipe; (5) nozzle.

2.3. Fresh State Properties

The fresh density of the mixture was measured using a standardized 1 L cylinder. The mixture was compacted in two layers and then weighed according to EN 12350-6 [23]. Flow table measurements were performed according to the EN 1015-3 standard [24]. Both tests were conducted before printing, approximately 15 min after adding water to the dry mix.

The initial and final setting time was measured using the Vicat method according to the EN 196-3 standard [25].

The yield stress of the tested material was determined by performing a rheometer test and slugs test. First, the rheometer test was carried out. A rheometer, "Schleibinger Viskomat XL" by Schleibinger Geräte Teubert u. Greim GmbH (Buchbach, Germany) for mortar and concrete, equipped with a Vane probe, was used to determine the dynamic yield stress and viscosity of the mixture. To study the setting process of the mixture over time, a periodically rotating and resting mode was set. The rheometer periodically rotated at 7 rpm for 1 min, followed by resting periods of either 6 or 11 min (Figure 2a). It should be noted that during the breaks between the rotation periods, no remixing or any impact on the mixture occurred.

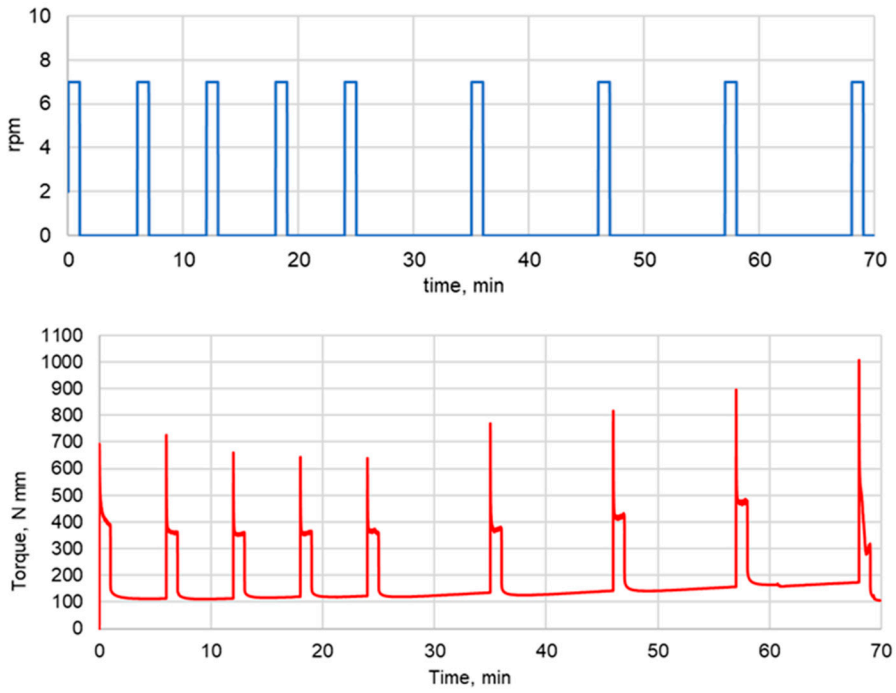

Figure 2. (**a**) Rheometer working protocol. The protocol consists of two parts with varying resting intervals: an initial resting phase of 6 min, followed by 1 min working time. After 25 min, the resting time extends to 11 min, followed by 1 min working time. (**b**) Rheological chart: time vs. torque.

During rheometer working periods, continuous measurements of the torque were carried out. The obtained rheological chart (Figure 2b) determined both static and dynamic yield stress. The dynamic yield stress represents the yield stress of a 3D-printed mixture under continuous shearing. In turn, the static yield stress corresponds to the yield stress of an undisrupted mixture after a resting period.

Shear stresses were determined using formulas provided in the user manual of the used rheometer:

$$\tau_0 = M/\left[2\pi R^3\right)\cdot(L/R + 2/3)] \quad (1)$$

where τ_0 is the shear stress (Pa), either dynamic or static; R is the radius of the used Vane probe, taken as 34.5 mm; L is the length of the used Vane probe, taken as 69.0 mm; and M is the torque (Nmm) obtained from the rheological chart.

The slugs test was used to determine the approximate yield stress of the material directly after extruding through a nozzle. The test involves extruding the material through a nozzle with a constant force until a slug (droplet) forms due to uniaxial yielding. To prepare for this test, a small bucket was placed on a scale under the printhead. The material was then loaded into the printhead and the printer was started at the intended extrusion

speed, approximately 50 cm above the bucket. The material was extruded into the bucket until it became homogeneous and slugs fell at roughly uniform intervals, appearing visually similar in length and shape. At this point, the scale was tared and the number of falling slugs was counted manually. Twenty-five slugs were counted to ensure a reliable result. At the end of the test, the total mass of the slugs was recorded and the average yield stress value was determined from the results [26,27].

A good printability can be considered to be achieved if the mixture is simultaneously buildable, pumpable, and extrudable, the layer geometry does not differ significantly between layers, and the surface quality is satisfactory [28]. All these parameters can be assessed simultaneously only through direct buildability tests by printing an actual object. Therefore, right after the slugs test, a direct buildability test was performed.

There are two possible types of fresh mass collapse in a printed object: elastic buckling due to loss of stability and plastic collapse due to exceeding the yield stress. Elastic buckling depends on the geometry of the printed object and the modulus of elasticity of the fresh mass. In contrast, geometry has minimal influence on plastic collapse, which mainly depends on the material used and its yield stress. Plastic collapse occurs when the vertical stresses from the mass's self-weight exceed the allowable shear stresses or yield stresses, causing the mass to flow laterally upon collapse [29–31]. A cylinder with a diameter of 250 mm was selected for the direct buildability test. This shape was chosen for its stable geometry, which delays buckling and favors plastic collapse over elastic.

By analyzing the fresh state properties, the material behavior during the 3D printing process was assessed, including its flowability, extrudability, and buildability. These properties will impact the layer adhesion and material's mechanical and durability performance. The following sections describe the mechanical and durability testing procedures for both printed and cast specimens.

2.4. Mechanical Testing

For the mechanical tests, both printed and cast samples were prepared. In order to prepare the printed samples, an object (Figure 3a) consisting of 1 horizontally adjacent filament and 24 vertical layers was printed. Each layer was approximately 10 mm in height and 50 mm wide.

The cast samples for flexural and compressive strength tests were made from the same batch as the printed object. The samples were prepared according to standard EN 1015-11 [32] using prismatic molds with dimensions of 40 × 40 × 160 mm.

Curing was divided into two stages: initial and normal curing. During initial curing, specimens were covered with airtight foil immediately after printing and stored for the first ~60 h, maintaining the conditions (T = 20 °C ± 2 °C; RH ≥ 95%). Later, during normal curing setup, the specimens were stored in water till the testing day.

After the curing period, the printed samples were sawn to 40 × 40 × 40 mm cubes for compressive strength (Figure 4) and splitting strength (Figure 5) tests, and 40 × 40 × 160 mm prisms for flexural strength tests (Figure 6). The samples were sawn by following specific directions from [17] on the specimen location. Part of the prismatic cast samples were sawn into cubes with dimensions of 40 × 40 × 40 mm for the compressive and splitting strength tests as well. To ensure flat parallelism of the bearing faces for test specimens, the planned cutting lines were manually marked on printed object parts by drawing them parallel or perpendicular to the bottom plane, which was confirmed to be completely flat (Figure 3b). During the sawing process, flat parallelism was maintained using the circular saw table, which was equipped with metal guides fixed perpendicular and parallel to the saw blade (Figure 3c). Once all the samples were prepared, they were visually inspected and, if necessary, all of the specimen faces subjected to compression were grinded to achieve an optimal surface quality for testing.

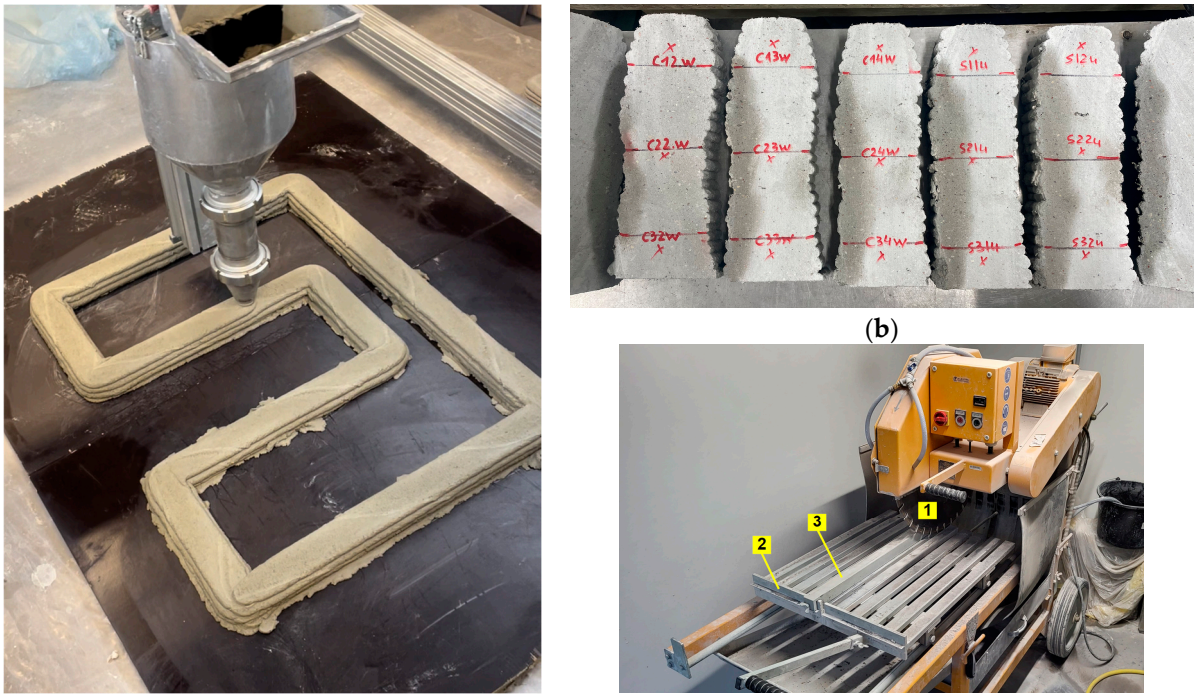

Figure 3. Specimen preparation for mechanical tests: (**a**) print object geometry for mechanical tests; (**b**) markings on specimens before cutting; (**c**) circular saw table: (1) circular saw blade; (2) metal guide fixed perpendicular to the saw blade; (3) metal guide fixed parallel to the saw blade.

The prepared samples were tested after 28 days of curing. Compressive and three-point bending strength tests were carried out. The compressive strength test was carried out using testing machine "Controls 50-C56Z00" from Controls S.p.A. (Milan, Italy). The test speed was set at 2400 N/s. Flexural strength tests were carried out using testing machine "Zwick Z100" from ZwickRoell GmbH & Co. (Ulm, Germany). The test speed was set at 50 N/s and 125 N/s for the flexural and splitting tests, respectively.

For the compressive strength tests, the cast samples (n = 9) were tested as reference samples and the printed samples were tested for three different directions in relation to print direction (Figure 4):

u direction—load applied perpendicular to the v,w plane (n = 9);
v direction—load applied perpendicular to the u,w plane (n = 9);
w direction—load applied perpendicular to the u,v plane (n = 9).

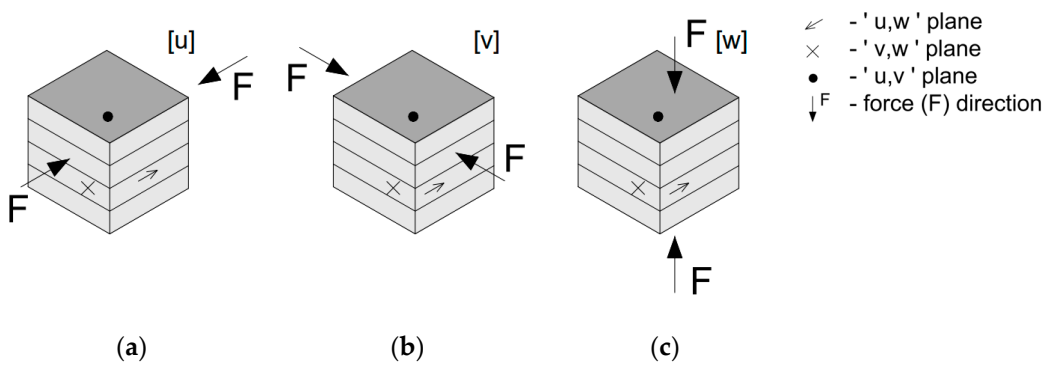

Figure 4. Test setups for compressive strength tests in various directions: (**a**) direction [u]; (**b**) direction [v]; (**c**) direction [w].

For the splitting strength tests, the cast samples (n = 9) were tested as reference samples and the printed samples were tested for three different directions in relation to print direction (Figure 5):

w/u direction—load applied parallel to print direction (n = 9);
v/w direction—load applied perpendicular to the top plane (n = 9);
u/v direction—load applied perpendicular to the side plane (n = 9).

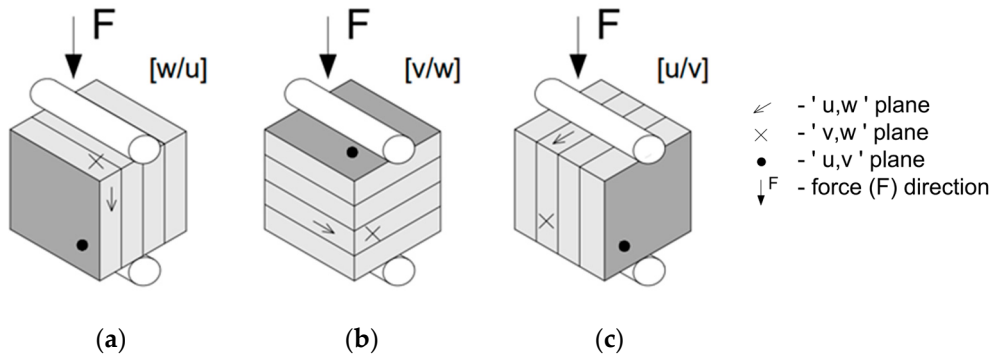

Figure 5. Test setups for splitting strength tests in various directions: (**a**) direction [w/u]; (**b**) direction [v/w]; (**c**) direction [u/v].

For the three-point flexural strength tests, the cast samples (n = 5) were tested as reference samples and the printed samples were tested for three different directions in relation to print direction (Figure 6):

u.w direction—load applied parallel to print direction (n = 7);
v.u direction—load applied perpendicular to the top plane (n = 7);
w.u direction—load applied perpendicular to the side plane (n = 7).

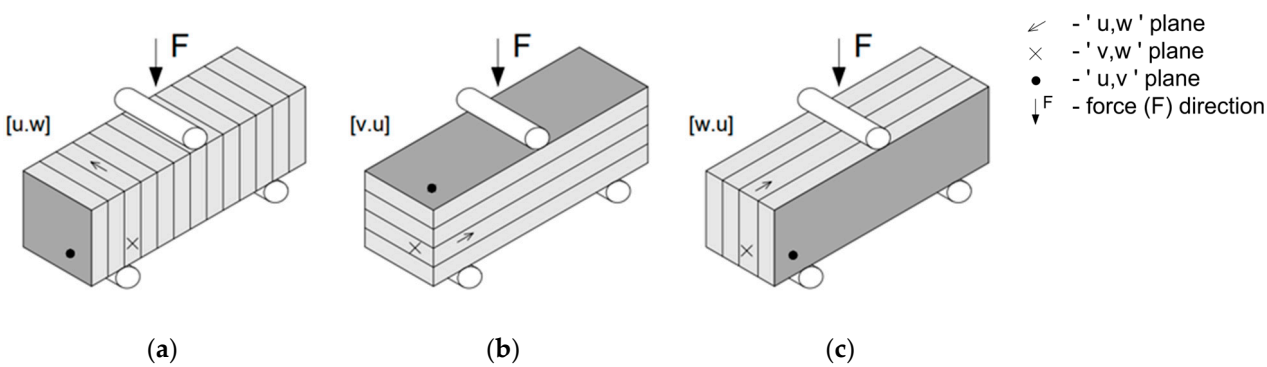

Figure 6. Test setups for flexural strength tests in various directions: (**a**) direction [u.w]; (**b**) direction [v.u]; (**c**) direction [w.u].

The assigned sample orientation names are described in detail in the study plan [17]. For each compressive and splitting test series, 9 samples were tested, from which every 3 specimens were taken from 3 different height locations—bottom, middle, and top section of the printed object. However, all the flexural strength series samples were extracted from the middle part of the print object.

2.5. Durability Testing

For the durability tests, both printed and cast samples were prepared according to the study plan [17]. In order to prepare the printed samples, two print objects with identical geometry (Figure 7), consisting of 1 horizontally adjacent filament and 6 vertical layers, were printed. Each layer was approximately 10 mm in height and 50 mm wide. The total

print path length of each object in the horizontal plane was 1500 mm, the material extrusion rate was 0.45 dm^3/min, and the vertical layer interval time was 20 s. The first object was printed without any additional time gap between any of the six layers. Samples obtained from this object were marked as T_0. For the second object, the initial three bottom layers were printed first. After a time gap equal to the initial setting time of 178 min, the remaining three layers were printed. This way, a cold joint was created in the middle of the print object. Samples obtained from this print object were marked as T_{SET}.

The cast samples for durability tests were made from the same batch as the printed object. The cast samples were prepared according to EN 1015-11 [32], using prismatic molds with dimensions of 40 × 40 × 160 mm.

Curing was divided into two stages: initial (see Section 2.4.) and normal curing. During normal curing setup, the specimens were stored under controlled conditions to maintain relative humidity of 60% and air temperature of ~18 °C until the testing day.

Contrary to the mechanical test specimens, the samples for durability tests were prepared by sawing the print objects only in the vertical direction. This way, test specimens with dimensions of 40 × 60 × 50 mm were obtained, with 60 mm and 50 mm being the unaltered height and width of the print object, respectively.

Figure 7. Print object geometry for durability tests. Two printed objects: the bottom part was printed first for the object with the cold joint (T_{SET}); the printed object without the cold joint (T_0).

After 28 days of curing, all durability samples were placed into a drying oven set at a temperature of 40 °C and dried until constant mass. Afterwards, each sample was coated with two layers of epoxy resin. For the water absorption tests, 4 out of 6 planes were coated, while for the carbonation tests, 5 out of 6 planes were coated.

Water absorption tests were carried out for 5 different test series as follows:

- T_0 with the side planes left uncoated (n = 3);
- T_0 with the top and bottom planes left uncoated (n = 3);
- T_{SET} with the side planes left uncoated (n = 3);
- T_{SET} with the top and bottom planes left uncoated (n = 3);
- Cast samples with two of the molded planes left uncoated (n = 3).

The dried water absorption samples were weighed, then put inside a water tank prepared according to the EN 1936 standard [33]. Samples were removed from the water tank after 1 min, wiped, and weighed. They were then immediately submerged back into the water. This procedure was repeated when the timer reached 3, 7, 15, 30, 60, 120, 180, 240, 300, 360, 1440, and 8640 min. The timer was stopped every time the weighing process was conducted.

Carbonation tests were carried out on 3 different test series as follows:

- Without the cold joint, T_0 with one of the side planes left uncoated (day 7, 28, 56, and 90, n = 3 for each day);

- With the cold joint, T_{SET} with one of the side planes left uncoated (day 7, 28, 56, and 90, n = 3 for each day);
- Cast samples with two of the molded planes left uncoated (day 7, 28, 56, and 90, n = 3 for each day).

The dried samples were placed inside a carbonation chamber with a desired carbonation level of 1%, relative humidity of 60%, and a temperature of 20 °C. After 7, 28, 56, and 90 days of exposure, samples were split in half. Samples were split using testing machine "Controls 50-C56Z00" from Controls S.p.A. (Italy), placing a wire at the top and bottom of the sample. Samples were split perpendicular to their uncoated surface.

Afterwards, a 1% phenolphthalein solution was sprayed on the freshly broken surfaces. Then, each of the broken surfaces was photographed alongside a millimeter paper to include a scale. Then each photo was processed using image analysis software ImageJ 1.8.0. For the cast samples, the carbonation depth was measured across the entire sample height, with measuring points placed every 2 mm. At each 2 mm interval in height, three points were picked on the photo to indicate the outer boundaries of the sample and the boundary between the carbonated and non-carbonated area. For the printed samples, the carbonation depth was only measured between the second and fifth layer, excluding the first and last layer to avoid side effects. Measuring points were placed following the same procedure as with the cast samples.

3. Results and Discussion

Having established the testing procedures and materials in Section 2, this chapter presents the results obtained from these tests. It includes an analysis of the fresh properties, as well as the mechanical and durability characteristics of both printed and cast specimens, followed by a discussion of their performance under various conditions.

3.1. Fresh Properties

Prior to 3D printing and 10 min after adding water to the dry mixture, fresh properties were assessed, as described in Section 2.3. The density of the fresh mixture was found to be 2040 kg/m^3. The flow table test showed a spread diameter of 165 mm after 15 jolts, indicating that the consistency of the mix was theoretically suitable for 3D printing [34]. The slugs test results revealed that the yield stress of the mixture was 1070 Pa, which falls within the acceptable range for printable materials for the particular 3D printer that was used and described in Section 2.3. Consequently, the consistency of the mixture was deemed acceptable, and the direct buildability test was started immediately after the slugs test, without adding any extra water.

Analyzing the obtained rheometer results, it can be observed that the static yield stress is nearly twice as high as the dynamic shear stress (Figure 8). The difference between static yield stress and dynamic shear stress reflects the thixotropic behavior of the 3D printing mixture. This phenomenon can be explained by the formation of temporary colloidal bonds during the resting phase, which are disrupted once movement begins. Both parameters are important for the 3D printing process: the dynamic yield stress affects both the required pumping pressure and the shape retention of the freshly laid layer, while the static yield stress determines the resistance against material failure.

When examining the results, it is evident that both static and dynamic yield stresses remain stable during the first 25 min of the test. After this period, there is an increase in these parameters, which is associated with the beginning of setting processes in the cement mixture. After 68 min, there was a sharp decrease in dynamic yield stress. This can be explained by the formation of a sliding plane between the Vane probe and the mixture as the material begins to set.

The rheometer and slugs test provided similar shear yield stress values within the first 35 min after adding water to the dry mixture (Figure 8). This suggests that the slugs test, which is a relatively very simple method to determine materials yield stress, is a fairly reliable measurement of concrete yield stress during the early stages of its working time.

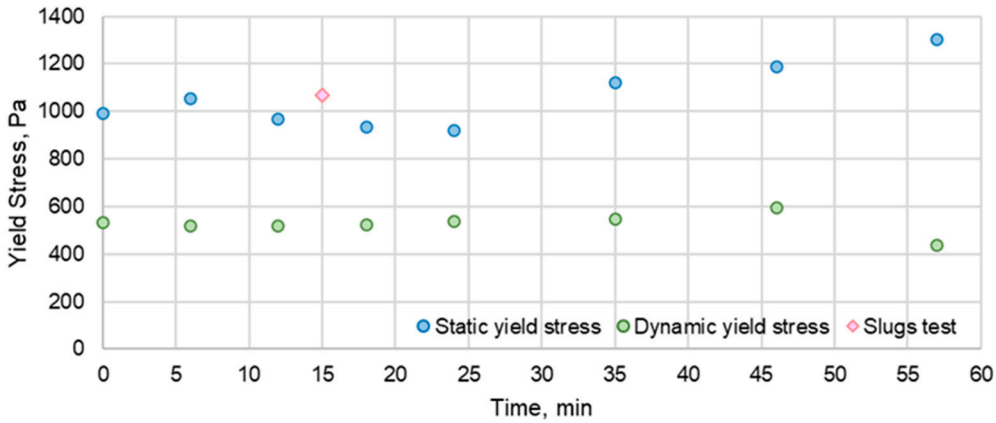

Figure 8. Static and dynamic yield stress values obtained via rheometer and slugs tests.

The direct buildability test was conducted 15 min after mixing the dry material with water. This test simultaneously evaluated the surface quality. The printing time for a single layer of the mixture was 6 s, with the total printing time for one object being approximately 2 min and 30 s. Therefore, the printing process spanned from the 15th to the 18th min after water was mixed into the dry material. It was possible to achieve a height of 18 layers, or 180 mm (Figure 9a), before experiencing plastic collapse (Figure 9b). It was calculated that at this stage, right before the collapse, the compressive strength of the fresh mixture was 3600 Pa.

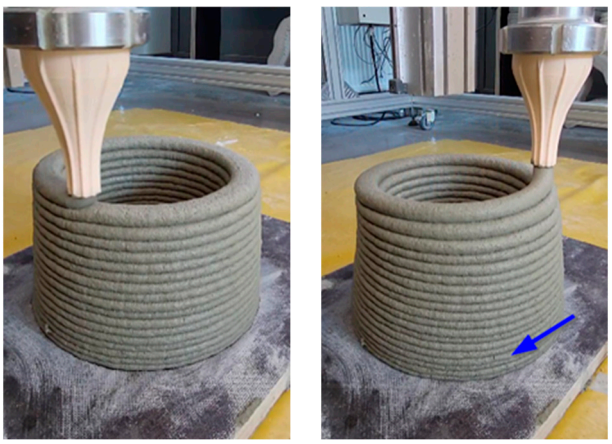

(**a**) (**b**)

Figure 9. Direct buildability test: (**a**) mixture right before plastic collapse; (**b**) plastic collapse.

Overall, the tests conducted on the mixture demonstrated its suitability for 3D printing. The surface quality of this mixture was acceptable, without any tearing or dimensional inconsistencies.

3.2. Mechanical Properties

3.2.1. Compressive Strength

Test results showed that none of the printed samples reached the same or higher compressive strength with respect to the cast samples, which was 37.8 MPa, comparable

to C30/37 standard concrete according to [35] (Figure 10). The printed samples overall showed lower values and demonstrated significant anisotropy in compressive strength depending on the loading direction.

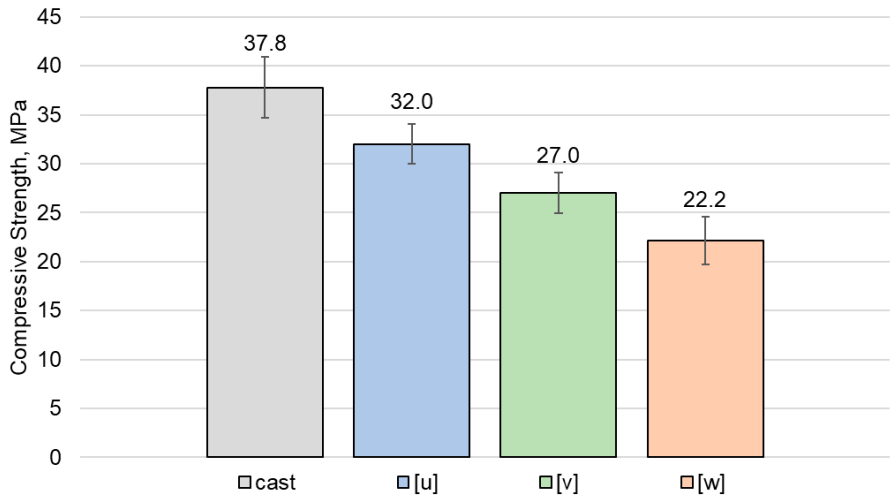

Figure 10. Compressive strength test results.

Among the printed samples, the highest compressive strength was observed in the [u] direction, where the load was applied parallel to the print layers, reaching approximately 85% of the cast sample strength.

Conversely, the samples tested in the [v] direction, where the load was applied perpendicular to the print object's side plane, exhibited lower compressive strength, reaching about 71% of the cast sample strength. The lower strength in the [v] direction is likely due to the minimal pressure applied in this direction during the setting process, allowing the concrete to settle and expand laterally without the confinement typically provided by formwork or molds [36].

The lowest compressive strength was recorded for the samples tested in the [w] direction, where the load was applied perpendicular to the print object's top plane, achieving only 59% of the cast sample strength. Self-weight of the concrete is the primary factor that compacts the concrete in the [w] direction [14]. While it provides some level of compaction, it is less effective compared to the high pumping pressure that compacts the concrete in the [u] direction.

While it is generally accepted that compressive and flexural strength tests do not give direct indication on interlayer bond strength, these results can give some insight on its quality. Most studies show that compressive strength is highest in the [u] direction, which is attributed to the higher density and closer packing of material which results from the high pumping pressure exerted during the extrusion of mortar [9].

However, when comparing the directions [w] and [v], results vary significantly across multiple studies. Some suggest that strength in the [w] direction surpasses strength in the [v] direction [9,17,37]. For 3D-printed concrete, this observation is not unexpected, as compression applied in the [v] direction—parallel to shear planes—can cause the specimens to separate or split along the interlayer regions [14]. As a result of this separation, multiple compression planes are formed instead of a single homogeneous one, thus weakening the entire specimen in the [v] direction.

At the same time, there are studies that indicate otherwise, reporting either similar or higher strength in [v] when compared to the [w] direction [14–16,38,39], which aligns with the results in this study. Here, and possibly in these other studies, the previously mentioned separation caused by insufficient interlayer bonding likely does not occur. Instead, the

compression plane remains intact across layers, avoiding the weakening effect that would typically lead to lower strength in the [v] direction compared to [w]. This suggests that good interlayer bonding plays an important role in maintaining the material's integrity under compressive loads.

In this study, the strong interlayer bond can be primarily attributed both to short interlayer times and over-extrusion. Over-extrusion in this case occurs when a 50 mm wide filament is printed using a 36 mm diameter nozzle. This results in the freshly extruded filament being slightly squeezed into the previous layer. This compression during deposition improves bonding between the layers, creating a stronger interlayer connection [40].

Future studies could investigate the specific role of interlayer bond strength in compressive strength across these two directions. For example, these tests could explore the effects of various interlayer times that intentionally weaken interlayer bonding or the effects of over-extrusion by varying the nozzle diameter.

However, while good interlayer bond strength convincingly explains why [v] is not weaker than [w], it does not explain why it is stronger. This suggests that additional factors, such as the material's microstructure, might contribute to the observed strength advantage in [v] direction. Since the objective of this study was to evaluate properties of this specific mixture using the given 3D printer, with the goal of establishing it as a benchmark mixture, rather than investigating the reasons behind directional differences, these aspects were not explored.

Comparison between compressive strength test results of samples taken from different height locations of the printed object—bottom, middle, and top—showed lower values for samples located in the top part (Figure 11).

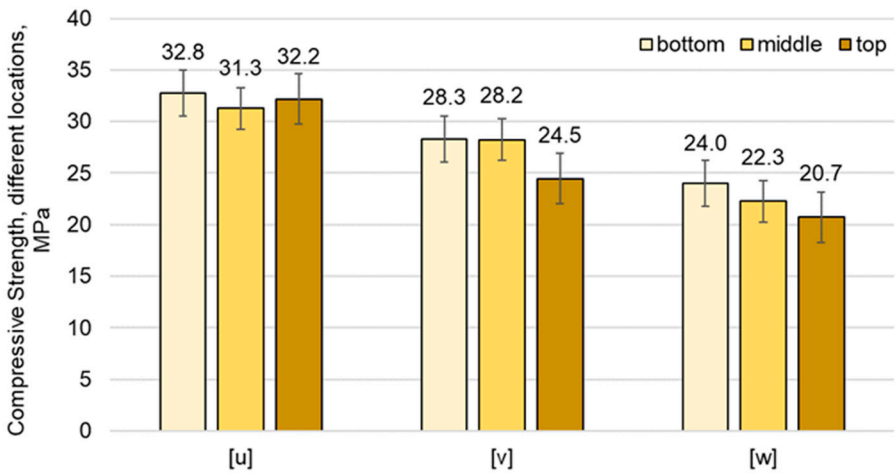

Figure 11. Comparison between compressive strength results of samples taken from different locations.

Interestingly, the [u] direction was least impacted by the height location. This suggests that compaction from the extruder in the direction of concrete deposition has the most influence on compressive strength, while the weight of concrete layers deposited on top has less influence in this direction. In contrast, the [v] direction exhibited, by 15%, lower compressive strength values for the samples taken from the top. However, within the range of standard deviation, the values were similar. The [w] direction was the only one that showed gradually decreasing values for the samples taken from the middle and top part, indicating that compaction from the self-weight of the layers plays a more crucial role in this direction, as expected.

Overall, the obtained compressive test results clearly show the anisotropy in the mechanical properties of 3D-printed concrete. The variability in strength values across different orientations and height locations emphasizes the need to consider the printing

direction when planning and designing 3D-printed concrete structures. Depending on the intended function and requirements of the designed structure, selecting the most appropriate printing direction is crucial.

Knowing the desired direction in which the structure will be used allows for evaluation and planning of which part of the structure (top/middle/bottom) should be utilized, or if it makes no difference. The desired direction for applying compression to the element is the [u] direction. In this direction, the compressive strength results are the highest, and it is of no particular concern which area of the printed element is subjected to the load more—strength is consistent throughout the entire height.

However, if the structure will be subjected to loads in the [w] direction, it is vital to recognize that this direction exhibits the lowest compressive strength compared to others, especially more towards the top part of the printed object. Therefore, when using the [w] direction, it is important to base calculations on the weakest sections to ensure structural integrity and safety.

3.2.2. Flexural Strength

Similar to the compressive strength test results, the flexural strength test results also indicate that the flexural strength of 3D-printed samples varies significantly depending on the direction of loading relative to the print layers (Figure 12).

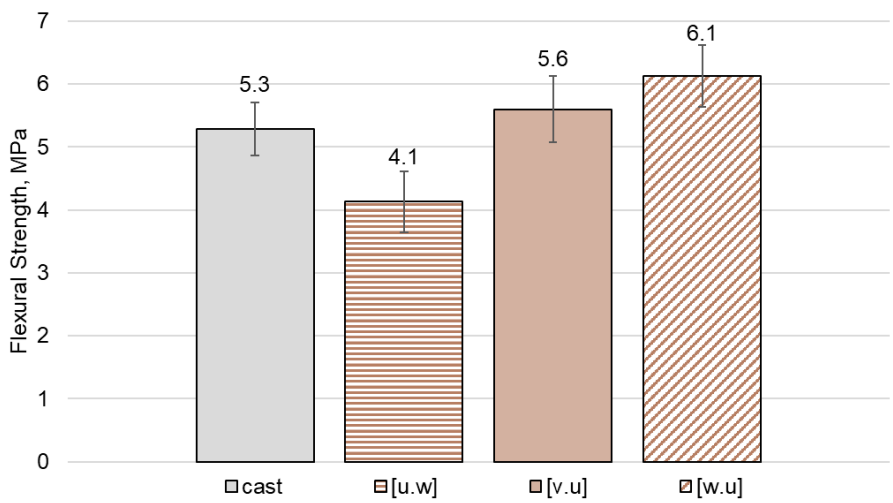

Figure 12. Flexural strength test results.

Clearly, the lowest flexural strength was observed in samples tested in the [u.w] direction, which is consistent with findings from previous studies [9,14,38]. Samples tested in the [u.w] direction exhibited a flexural strength that was only 77% of cast sample strength. In this direction, load was applied parallel to the layers, directly stressing the interfaces between the layers.

However, by visually observing the samples after flexural failure, it was noticed that the fracture line was not straight or clearly defined, suggesting that the failure did not happen only along the interlayer regions (Figure 13a). The scattered fracture pattern could indicate that the printed filaments merged during the printing process, likely due to the previously mentioned over-extrusion. It also suggests that the interlayer bond strength is relatively high, preventing clear separation along the interlayer regions. Both factors likely improve structural integrity of the test specimens, suggesting that the mixture and printing technology used in this study provide a structure with relatively strong interlayer bond strength.

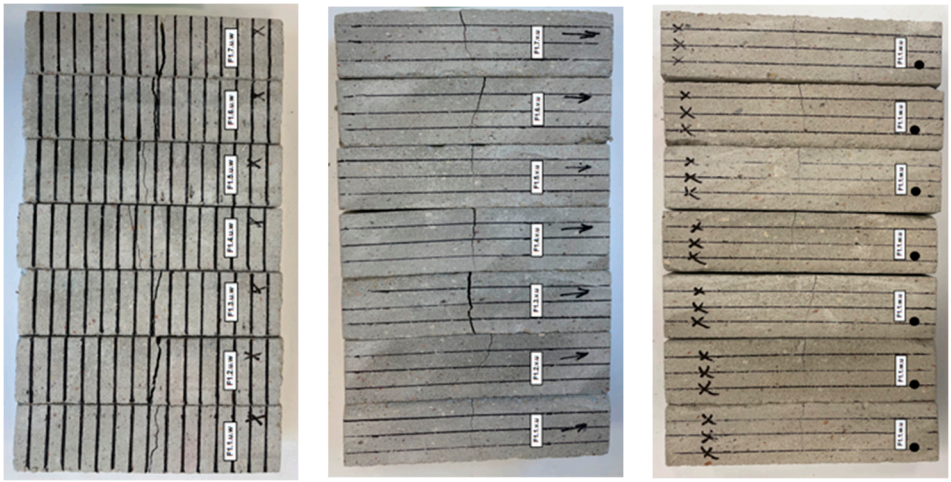

(**a**) (**b**) (**c**)

Figure 13. The fracture pattern of flexural strength test specimens: (**a**) direction [u.w]; (**b**) direction [v.u]; (**c**) direction [w.u].

Test results showed that samples tested in the [w.u] and [v.u] directions had, by 13% and 5%, higher flexural strength, respectively, than the cast samples. While there are slight differences in strength observed between these two directions, the overlap within the range of standard deviations suggests that they are minor, leading to comparable structural performance.

In contrast to the findings of this research, other studies have reported higher strength values in the [v.u] direction compared to the [w.u] direction [9,14,38]. Typically, the higher strength in the [v.u] direction is attributed to better compaction of the material due to self-weight. For instance, Panda et al. [9] suggested that specimens loaded in the [v.u] direction, taken from the bottom of a printed block, showed higher strength likely due to better compaction compared to specimens in the [w.u] direction. Since all the samples in this study were taken from the middle of the printed object, the effect of self-weight compaction was likely minimal, leading to the relatively small differences in flexural strength between the [w.u] and [v.u] directions observed in this study.

In practical applications, the specific direction of loading must be carefully considered when subjecting 3D-printed structures to flexural loads. If the structure is expected to be subjected to bending forces in the [u.w] direction, it may be necessary to reinforce the structure or adjust the orientation of the printed layers to more effectively distribute loads across areas with higher strength [41,42], such as the [w.u] or [v.u] directions. These directions demonstrated higher flexural strength and are more suitable for elements subjected to bending forces. Even though this study did not show pronounced separation in the interlayer region when tested in the [u.w] direction, the risk of failure along the interlayer is higher in this orientation. This risk could become more significant if a faulty layer is printed, which could lead to delamination.

3.2.3. Splitting Strength

The test results indicate that the splitting strength of the printed samples was approximately 10% lower compared to the cast samples (Figure 14). The direction of the applied load did not significantly affect the splitting strength of the printed samples, as the obtained strength differences were negligible. This uniformity in splitting strength is consistent with studies performed by other authors as well [15].

The fact that the printed material resists splitting equally well in all directions also indirectly indicates that the interlayer bond strength achieved with this specific mixture and print technology is relatively high.

In practical applications, the uniformity in splitting strength across all loading directions suggests that 3D-printed structures using this specific mixture and print technology can reliably resist tensile stresses regardless of orientation.

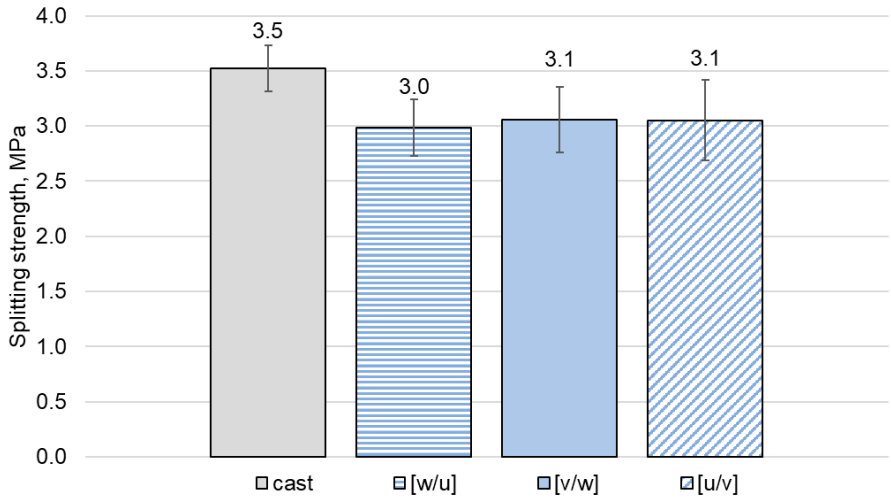

Figure 14. Splitting strength test results.

Although uniaxial compression tests, three-point bending tests, and splitting strength tests do not directly measure interlayer bonding strength, testing in three different directions has given valuable insights into the anisotropy of 3D-printed structures using this specific mixture and printing technology. The results reveal how the material's properties vary with the direction of the applied load and help determine the best orientation for structural use if such preference exists. At the same time, the material showed consistent performance regardless of direction, such as in splitting strength across all directions and minimal differences in flexural and compressive strength when comparing [v.u] to [w.u] and [v] to [w], respectively, which simplifies use in structural applications.

3.3. Durability Properties

3.3.1. Water Absorption

The water absorption test results revealed that all of the printed samples exhibited higher water absorption through the outer plane compared to the bottom plane (Figure 15). The simplest explanation for this difference could be attributed to the surface irregularities, as in this study, the surface area was measured as the distance between two planes and did not account for the actual surface texture, including the printed layer contours.

However, water absorption through the outer plane is likely greater not only due to surface irregularities but also because of the increased porosity along the interlayer regions, which facilitates greater water ingress [8,43]. Additionally, the morphology of pores in these interlayer regions changes, becoming flattened and therefore elongated [44,45]. As a result, when water exposure occurs from the side, these flattened and elongated pores are likely oriented in a way that promotes water infiltration in that direction.

In order to confirm this hypothesis, further research should be conducted, possibly including an analysis of sawn samples while excluding other factors such as texture cracks and the geometry of the printed elements. The water absorption from the side would likely show higher values due to the pores being more elongated in the direction of printing and sideways, which encourages water absorption along the layers rather than vertically, from

bottom to top. It should be noted that sawing the samples was not part of this study, as it is unlikely that samples are sawn after printing in practical scenarios.

Additionally, surface microcracks can lead to an increased capillary suction [8]. These cracks are more likely to form on the outer surface of printed elements, unlike the bottom plane, which was in contact with a plywood sheet, providing better curing conditions. The curing conditions on the outer surface could further explain the higher water absorption.

Although the water absorption results indicate that printed samples generally performed better than cast ones, this does not necessarily imply an overall improvement in durability. While the extrusion process may have compacted the material and reduced water absorption in some cases, it also introduced weak interlayer zones and increased overall permeability.

When comparing the printed samples with a cold joint (T_{SET}) to those without a cold joint (T_0), it becomes evident that the longer layer interval time in the T_{SET} samples leads to higher water absorption. This increased water absorption is attributed to the presence of a weak interlayer zone, which is more pronounced with extended layer interval times. This finding aligns with previous research [8,45] which has shown that longer delays between layer depositions weaken the interlayer bond. In these weak zones, the concrete does not bond as effectively, creating pathways for water to infiltrate more readily. The results indicate that minimizing the time interval between layers is crucial for reducing water absorption and ensuring the overall durability and performance of the 3D-printed structure.

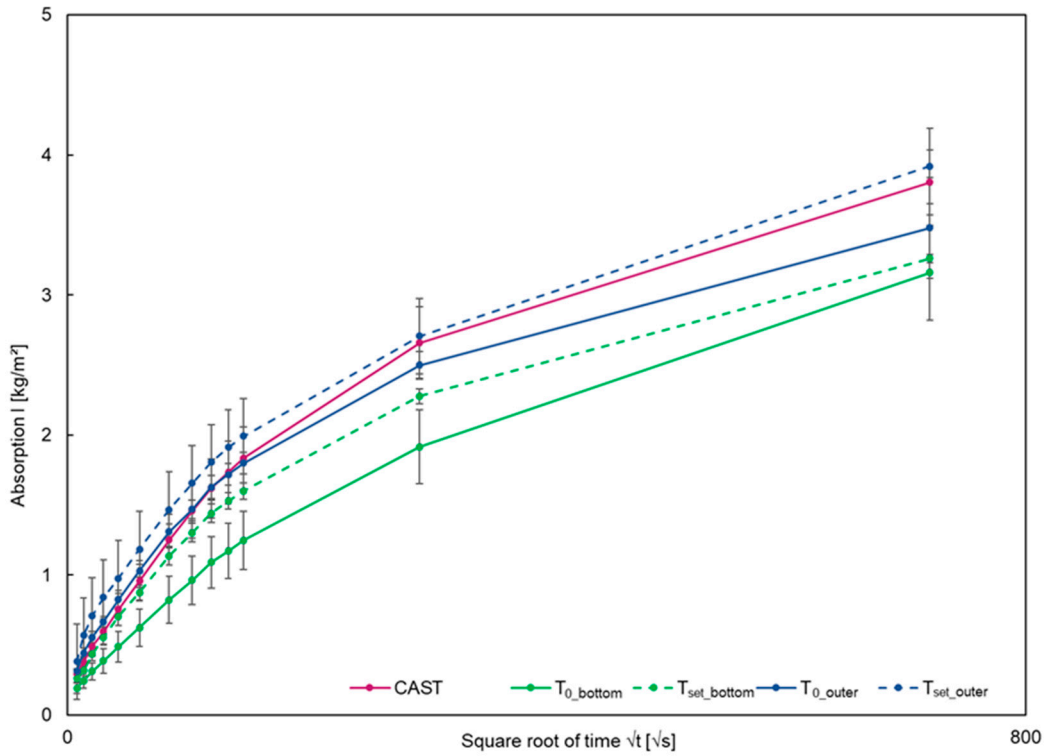

Figure 15. Water absorption test results.

3.3.2. Carbonation

When exposed to atmospheric conditions, carbonation will occur in concrete structures at a relatively slow but invasive pace. Initially, the high pH of concrete provides a protective environment for the steel reinforcement, preventing corrosion. However, carbonation leads to a reduction in the concrete's pH level and once the carbonation front reaches the reinforcement, the reduced pH level allows steel corrosion to begin. Corrosion reduces

the effective rebar section and causes spalling in the concrete as the corrosion products expand [5,46].

It is evident that the interlayer regions, which are more permeable than the intralayer regions, can cause a significantly faster rate of corrosion in the reinforcement within 3D-printed concrete elements. This increased permeability allows for easier penetration of carbon dioxide, which accelerates the carbonation process [46].

This issue is especially important in cases where the reinforcement is positioned horizontally between adjacent layers. In such cases, the enhanced rate of corrosion can compromise the structural integrity by causing delamination [5]. Delamination, the separation of layers in the concrete, can severely weaken the structural element, leading to potential failures and reduced durability of the 3D-printed concrete element. Therefore, understanding the permeability of interlayer regions and cold joints is crucial to ensuring the durability of reinforced 3D-printed concrete structures.

After the carbonation test, the photos taken were processed and the carbonation depth was measured (Figure 16). When comparing the cast samples to the printed elements without the cold joint (T_0) at earlier ages, the results show somewhat similar carbonation depth values. Overall, the carbonation depth is slightly higher for the printed samples than for the cast samples. This might be attributed to the slightly lower lateral compaction for printed samples when compared to the cast ones.

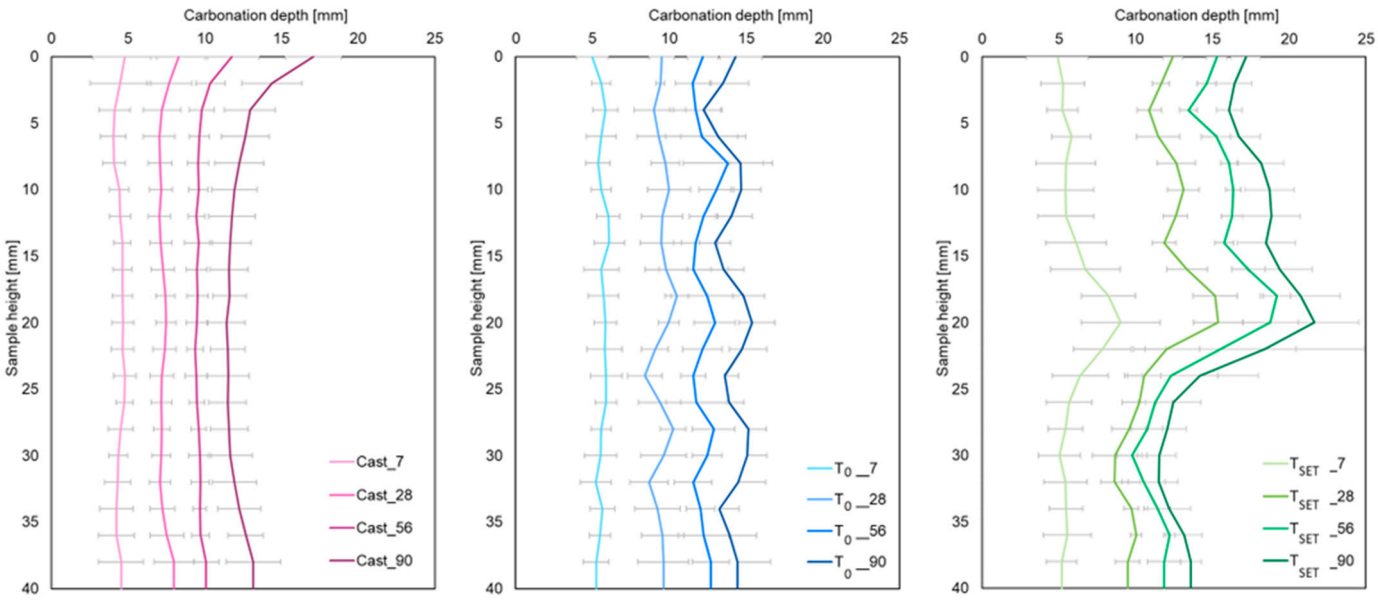

(**a**) (**b**) (**c**)

Figure 16. Carbonation depth of the developed mixture after 7, 28, 56, and 90 days for (**a**) cast samples; (**b**) printed samples without the cold joint (T_0); (**c**) printed samples with the cold joint (T_{SET}).

The relatively consistent depth of the carbonation front across the height of the printed elements without the cold joint (T_0) suggests that the interlayer regions are not acting as significant accelerators of the carbonation process (Figure 16b). Instead, the carbonation appears to be uniformly affecting the entire structure. This uniformity could be due to the particular properties of the 3D printing process, such as the short interlayer time, suitable ambient room conditions such as efficient humidity, protection from the sun and wind, and materials used, which may have created a more homogeneous and well-bonded structure than initially anticipated.

At the same time, the carbonation test results for the samples with the cold joint (T_{SET}) reveal that the cold joints in the printed concrete elements are severely affected by carbonation (Figure 16c). These joints, where the concrete layers meet but do not fully bond, provide pathways for carbon dioxide to penetrate more deeply and quickly, leading to an accelerated rate of carbonation in these areas.

By visually observing the carbonation samples without the cold joint, it was apparent that for the samples tested at earlier ages (7, 28, and 56 days), the carbonation front followed the actual geometry of the printed layers (Figure 17a–c). However, at later ages (90 days), the carbonation front no longer mimics the actual geometry of the printed layers but moves in a more uniform, straight-line pattern instead (Figure 17d). This suggests that the initial layer-by-layer geometry is less influential towards the middle, where the older concrete layer more effectively blended with the newly printed layer, creating a more uniform interlayer region. Additionally, the slower evaporation of water in the middle sections of the concrete likely contributed to this protective effect. Overall, this shows that over longer periods of time when the carbonation front has moved more towards the middle, the interlayer regions are less influential.

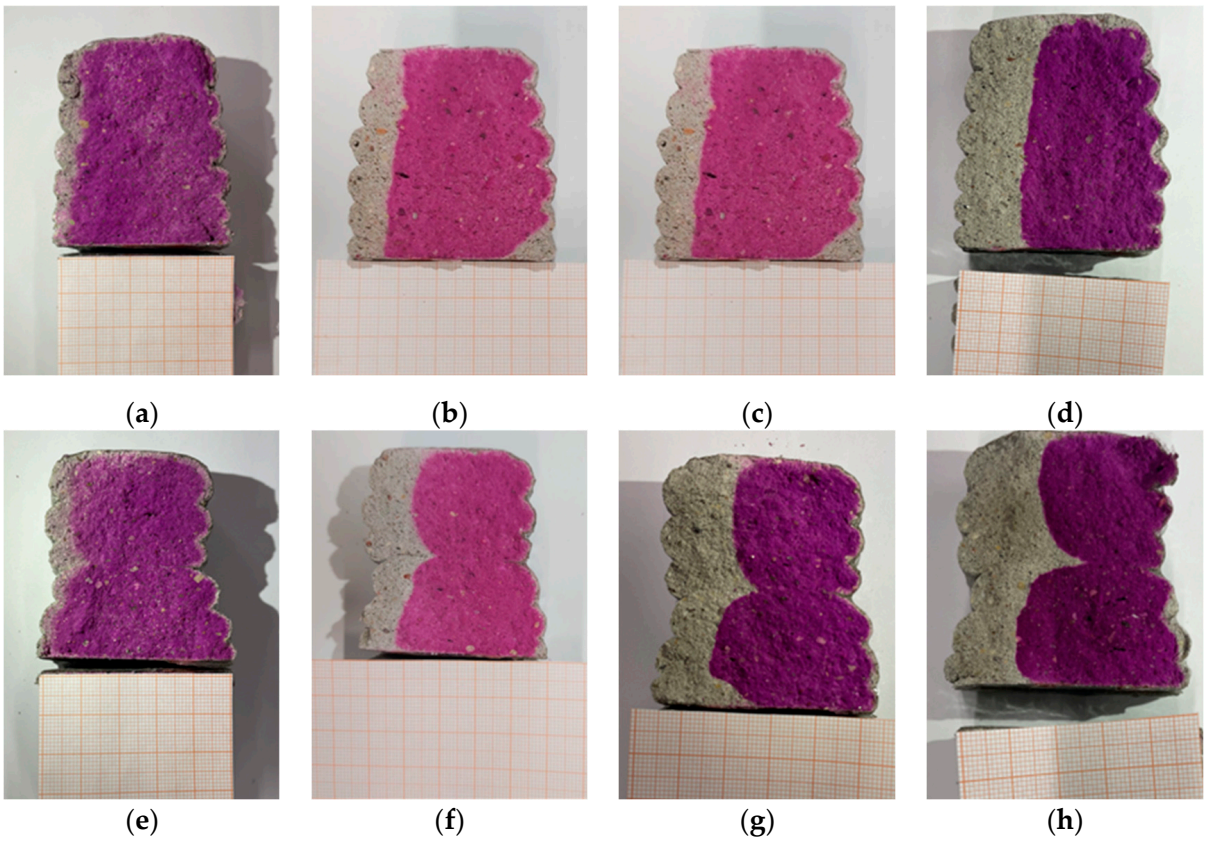

Figure 17. 3D-printed carbonation samples after testing: (**a**) T_0 after 7 days; (**b**) T_0 after 28 days; (**c**) T_0 after 56 days; (**d**) T_0 after 90 days; (**e**) T_{SET} after 7 days; (**f**) T_{SET} after 28 days; (**g**) T_{SET} after 56 days; (**h**) T_{SET} after 90 days.

Interestingly, while the interlayer geometry becomes less apparent over time, the cold joint remains clearly visible even after 90 days (Figure 17h). This demonstrates that while the interlayer regions integrate over time and more towards the core of the sample, the cold joint continues to act as a clear boundary within the material.

Findings of this test clearly show that a short interlayer time does not significantly affect carbonation, but a long interlayer time greatly accelerates the process. When the time

between applying concrete layers is short, the layers can bond more effectively, creating a more uniform and less porous structure that is more resistant to carbonation.

In contrast, if the interval between applying layers is long, the layers do not bond as well, resulting in weaker interlayer zones. These zones are more vulnerable to the ingress of carbon dioxide, which accelerates the carbonation process. Consequently, a long interlayer time can create significant weak points in the structure, promoting faster corrosion of the concrete and reducing its durability. This highlights the importance of controlling the time between layer applications in 3D-printed concrete to ensure high resistance to carbonation and long-term structural stability.

The findings of this study highlight specific durability risks associated with 3D printing technology, such as the negative influence of cold joints and the increased surface area resulting from the textured geometry of printed layers. Since industry standards favor low water absorption and minimal carbonation depth to ensure the long-term performance of concrete structures, these aforementioned risks must be carefully evaluated before exposing the structure to real-life environmental conditions.

4. Conclusions

The tested mixture demonstrated good printability and sufficient buildability, achieving 18 layers before experiencing plastic collapse. A good printability window was identified between the 15th and 35th min after mixing, during which the static yield stress of the mixture was around 1000 Pa and the dynamic yield stress was around 550 Pa. The optimal yield stress allows for printing with good surface quality, without tearing.

This study has confirmed the anisotropic nature of 3D-printed concrete. The compressive strength varied depending on the orientation of the applied load relative to the print layers. The highest strength was achieved when the load was applied parallel to print direction ([u] direction), reaching 85% of the cast sample strength. Lower strength was observed when the load was applied perpendicular to a print object's side plane ([v] direction) or perpendicular to the top plane ([w] direction), reaching only 71% and 59% of cast sample strength, respectively.

For flexural strength, the highest and relatively similar values were observed when load was applied perpendicular to print layers ([v.u] and [w.u] directions), reaching approximately 75% of the strength of cast samples. However, when the load was applied parallel to the print layers ([u.w] direction), flexural strength dropped significantly, achieving only 53% of the cast sample strength.

In terms of splitting tensile strength, the difference between print directions was less pronounced. Across all directions, the splitting tensile strength of printed samples reached about 90% of the cast sample strength.

Water absorption and carbonation tests indicated that the durability of 3D-printed concrete was significantly influenced by cold joints. Cold joints were more prone to water ingress and accelerated carbonation.

In the carbonation tests, samples without cold joints performed similarly to cast samples. In contrast, samples with cold joints displayed a noticeably faster moving carbonation front across the sample cross-section. This shows that interlayer regions have significantly smaller impact on durability compared to cold joints, especially near the center of the printed samples, where the carbonation front appeared more uniform. These findings suggest that the interlayer bond in samples using the concrete mixture described in this study, combined with the applied printing technology, is strong enough to minimize its influence on long-term durability, except when an actual cold joint is present.

The study's findings suggest that 3D-printed concrete can achieve comparable strength and durability to traditionally cast concrete, provided that care is taken to control interlayer time and conditions.

Author Contributions: Conceptualization M.Š. and A.S.; methodology F.P.B.; formal analysis M.Š., A.S. and G.Š.; investigation M.Š., A.S., G.Š., L.H., L.K.B. and K.Š.; writing—original draft preparation, A.S. and M.Š.; visualization, A.S.; software, S.R.; writing—review and editing, A.S., M.Š., L.K.B. and F.P.B.; data curation, A.S.; project administration, M.Š. and A.S.; funding acquisition, M.Š., D.B. and A.S. All authors have read and agreed to the published version of the manuscript.

Funding: A.S. was funded by Riga Technical University 2023/2024 Project for Strengthening Scientific Personnel Capacity Nr. ZM-2024/25, grant number B59, ID 4826. This research was funded by Riga Technical University 2024 Project for Scientist Grants RTU-ZG-2024/1-0008, "Low-CO2 concrete 3D printing using waste materials". The authors gratefully acknowledge the financial support of the Slovenian Research and Innovation Agency (research core funding No. P2 0273 and No. I0-0032).

Data Availability Statement: The datasets presented in this article are not readily available because the data are part of an ongoing study which is conducted under RILEM committee 304-ADC, Assessment of Additively Manufactured Concrete Materials and Structures. Requests to access the datasets should be directed to the chair of this committee.

Acknowledgments: To the organizers of RILEM technical committees 304-ADC: Assessment of Additively Manufactured Concrete Materials and Structures and 303-PFC: Performance Requirements and Testing of Fresh Printable Cement-Based Materials, as well as authors of guidelines used in this study.

Conflicts of Interest: The authors declare no conflicts of interest.

References

1. Ye, J.; Cui, C.; Yu, J.; Yu, K.; Xiao, J. Fresh and anisotropic-mechanical properties of 3D printable ultra-high ductile concrete with crumb rubber. *Compos. Part B Eng.* **2021**, *211*, 108639. [CrossRef]
2. Malik, U.J.; Riaz, R.D.; Rehman, S.U.; Usman, M.; Riaz, R.E.; Hamza, R. Advancing mix design prediction in 3D printed concrete: Predicting anisotropic compressive strength and slump flow. *Case Stud. Constr. Mater.* **2024**, *21*, e03510. [CrossRef]
3. Hou, S.; Duan, Z.; Xiao, J.; Ye, J. A review of 3D printed concrete: Performance requirements, testing measurements and mix design. *Constr. Build. Mater.* **2021**, *273*, 121745. [CrossRef]
4. Munemo, R.; Kruger, J.; van Zijl, G.P.A.G. Improving interlayer bond in 3D printed concrete through induced thermo-hydrokinetics. *Constr. Build. Mater.* **2023**, *393*, 132121. [CrossRef]
5. Kruger, J.; van Zijl, G. A compendious review on lack-of-fusion in digital concrete fabrication. *Addit. Manuf.* **2021**, *37*, 101654. [CrossRef]
6. Moelich, G.M.; Kruger, J.; Combrinck, R. Modelling the interlayer bond strength of 3D printed concrete with surface moisture. *Cem. Concr. Res.* **2021**, *150*, 106559. [CrossRef]
7. Van Der Putten, J.; De Schutter, G.; Van Tittelboom, K. The Effect of Print Parameters on the (Micro)structure of 3D Printed Cementitious Materials. In Proceedings of the First RILEM International Conference on Concrete and Digital Fabrication—Digital Concrete, Zurich, Switzerland, 10–12 September 2018; Springer International Publishing: Cham, Switzerland, 2019; pp. 234–244. [CrossRef]
8. Van Der Putten, J.; De Volder, M.; Van den Heede, P.; Deprez, M.; Cnudde, V.; De Schutter, G.; Van Tittelboom, K. Transport properties of 3D printed cementitious materials with prolonged time gap between successive layers. *Cem. Concr. Res.* **2022**, *155*, 106777. [CrossRef]
9. Panda, B.; Paul, S.C.; Tan, M.J. Anisotropic mechanical performance of 3D printed fiber reinforced sustainable construction material. *Mater. Lett.* **2017**, *209*, 146–149. [CrossRef]
10. Cicione, A.; Kruger, J.; Walls, R.S.; Van Zijl, G. An experimental study of the behavior of 3D printed concrete at elevated temperatures. *Fire Saf. J.* **2021**, *120*, 103075. [CrossRef]
11. Moini, M.; Olek, J.; Magee, B.; Zavattieri, P.; Youngblood, J. Additive Manufacturing and Characterization of Architectured Cement-Based Materials via X-ray Micro-computed Tomography. In Proceedings of the First RILEM International Conference on Concrete and Digital Fabrication–Digital Concrete, Zurich, Switzerland, 10–12 September 2018; Springer International Publishing: Cham, Switzerland, 2019; pp. 176–189. [CrossRef]

12. Moelich, G.M.; Kruger, P.J.; Combrinck, R. The effect of restrained early age shrinkage on the interlayer bond and durability of 3D printed concrete. *J. Build. Eng.* **2021**, *43*, 102857. [CrossRef]
13. Van Der Putten, J.; De Volder, M.; Van den Heede, P.; De Schutter, G.; Van Tittelboom, K. 3D Printing of Concrete: The Influence on Chloride Penetration. In *RILEM International Conference on Concrete and Digital Fabrication*; Springer International Publishing: Cham, Switzerland, 2020; pp. 500–507. [CrossRef]
14. Nerella, V.N.; Hempel, S.; Mechtcherine, V. Effects of layer-interface properties on mechanical performance of concrete elements produced by extrusion-based 3D-printing. *Constr. Build. Mater.* **2019**, *205*, 586–601. [CrossRef]
15. Wolfs, R.J.M.; Bos, F.P.; Salet, T.A.M. Hardened properties of 3D printed concrete: The influence of process parameters on interlayer adhesion. *Cem. Concr. Res.* **2019**, *119*, 132–140. [CrossRef]
16. Paul, S.C.; Tay, Y.W.D.; Panda, B.; Tan, M.J. Fresh and hardened properties of 3D printable cementitious materials for building and construction. *Arch. Civ. Mech. Eng.* **2018**, *18*, 311–319. [CrossRef]
17. Bos, F.; Mechtcherine, V.; Roussel, N.; Menna, C.; Wolfs, R.; Lombois-Burger, H.; Baz, B.; Weger, D.; Moro, S.; Nematollahi, B.; et al. *RILEM TC 304-ADC ILS-mech Study Plan*; Technical University of Munich: Munich, Germany, 2023. [CrossRef]
18. Kränkel, T.; Van Tittelboom, K.; Van Der Putten, J. *RILEM TC 304-ADC ILS-DURASHRINK Study Plan*; Technical University of Munich: Munich, Germany, 2023.
19. Jiao, D.; Shi, C.; Yuan, Q.; An, X.; Liu, Y.; Li, H. Effect of constituents on rheological properties of fresh concrete—A review. *Cem. Concr. Compos.* **2017**, *83*, 146–159. [CrossRef]
20. Marchon, D.; Kawashima, S.; Bessaies-Bey, H.; Mantellato, S.; Ng, S. Hydration and rheology control of concrete for digital fabrication: Potential admixtures and cement chemistry. *Cem. Concr. Res.* **2018**, *112*, 96–110. [CrossRef]
21. Khayat, K.H. Effects of Antiwashout Admixtures on Fresh Concrete Properties. *ACI Mater. J.* **1995**, *92*, 164–171. [CrossRef]
22. Chen, B.; Liu, J. Contribution of hybrid fibers on the properties of the high-strength lightweight concrete having good workability. *Cem. Concr. Res.* **2005**, *35*, 913–917. [CrossRef]
23. *EN 12350-6:2019*; Testing Fresh Concrete—Part 6: Density. European Committee for Standardization: Brussels, Belgium, 2019.
24. *EN 1015-3:2000*; Methods of Test for Mortar for Masonry—Part 3: Determination of Consistence of Fresh Mortar (by Flow Table). European Committee for Standardization: Brussels, Belgium, 1999.
25. *EN 196-3:2016*; Methods of Testing Cement—Part 3: Determination of Setting Times and Soundness. European Committee for Standardization: Brussels, Belgium, 2016.
26. Ducoulombier, N.; Carneau, P.; Mesnil, R.; Demont, L.; Caron, J.-F.; Roussel, N. 'The Slug Test': Inline Assessment of Yield Stress for Extrusion-Based Additive Manufacturing. In *Second RILEM International Conference on Concrete and Digital Fabrication*; Springer International Publishing: Cham, Switzerland, 2020; pp. 216–224. [CrossRef]
27. Nicolas, R.; Dirk, L. *303-PFC: Performance Requirements and Testing of Fresh Printable Cement-Based Materials*; RILEM Technical Committee: Paris, France, 2021.
28. Kazemian, A.; Yuan, X.; Cochran, E.; Khoshnevis, B. Cementitious materials for construction-scale 3D printing: Laboratory testing of fresh printing mixture. *Constr. Build. Mater.* **2017**, *145*, 639–647. [CrossRef]
29. Kruger, J.; Zeranka, S.; van Zijl, G. 3D concrete printing: A lower bound analytical model for buildability performance quantification. *Autom. Constr.* **2019**, *106*, 102904. [CrossRef]
30. Ivanova, I.; Ivaniuk, E.; Bisetti, S.; Nerella, V.N.; Mechtcherine, V. Comparison between methods for indirect assessment of buildability in fresh 3D printed mortar and concrete. *Cem. Concr. Res.* **2022**, *156*, 106764. [CrossRef]
31. Suiker, A.S.J.; Wolfs, R.J.M.; Lucas, S.M.; Salet, T.A.M. Elastic buckling and plastic collapse during 3D concrete printing. *Cem. Concr. Res.* **2020**, *135*, 106016. [CrossRef]
32. *EN 1015-11:2019*; Methods of Test for Mortar for Masonry—Part 11: Determination of Flexural and Compressive Strength of Hardened Mortar. European Committee for Standardization: Brussels, Belgium, 2019.
33. *EN 1936:2006*; Natural Stone Test Methods—Determination of Real Density and Apparent Density, and of Total and Open Porosity. European Committee for Standardization: Brussels, Belgium, 2006.
34. Sahmenko, G.; Puzule, L.; Sapata, A.; Slosbergs, P.; Bumanis, G.; Sinka, M.; Bajare, D. Gypsum–Cement–Pozzolan Composites for 3D Printing: Properties and Life Cycle Assessment. *J. Compos. Sci.* **2024**, *8*, 212. [CrossRef]
35. *EN-1992-1-1:2024*; Eurocode 2—Design of concrete structures—Part 1-1: General rules and rules for buildings, bridges and civil engineering structures. European Committee for Standardization: Brussels, Belgium, 2024.
36. Sanjayan, J.G.; Nematollahi, B.; Xia, M.; Marchment, T. Effect of surface moisture on inter-layer strength of 3D printed concrete. *Constr. Build. Mater.* **2018**, *172*, 468–475. [CrossRef]
37. Zhang, Y.; Zhang, Y.; She, W.; Yang, L.; Liu, G.; Yang, Y. Rheological and harden properties of the high-thixotropy 3D printing concrete. *Constr. Build. Mater.* **2019**, *201*, 278–285. [CrossRef]
38. Le, T.T.; Austin, S.A.; Lim, S.; Buswell, R.A.; Law, R.; Gibb, A.G.; Thorpe, T. Hardened properties of high-performance printing concrete. *Cem. Concr. Res.* **2012**, *42*, 558–566. [CrossRef]

39. Mechtcherine, V.; Nerella, V.N.; Will, F.; Näther, M.; Otto, J.; Krause, M. Large-scale digital concrete construction—CONPrint3D concept for on-site, monolithic 3D-printing. *Autom. Constr.* **2019**, *107*, 102933. [CrossRef]
40. Elistratkin, M.; Alfimova, N.; Podgornyi, D.; Olisov, A.; Promakhov, V.; Kozhukhova, N. Influence of Equipment Operation Parameters on the Characteristics of a Track Produced with Construction 3D Printing. *Buildings* **2022**, *12*, 593. [CrossRef]
41. Zeng, J.-J.; Li, P.-L.; Yan, Z.-T.; Zhou, J.-K.; Quach, W.-M.; Zhuge, Y. Behavior of 3D-printed HPC plates with FRP grid reinforcement under bending. *Eng. Struct.* **2023**, *294*, 116578. [CrossRef]
42. Liao, J.; Yang, K.Y.; Zeng, J.-J.; Quach, W.-M.; Ye, Y.-Y.; Zhang, L. Compressive behavior of FRP-confined ultra-high performance concrete (UHPC) in circular columns. *Eng. Struct.* **2021**, *249*, 113246. [CrossRef]
43. Anleu, P.C.B. *Quantitative Micro XRF Mapping of Chlorides: Possibilities, Limitations, and Applications, from Cement to Digital Concrete*; ETH Zurich: Zürich, Switzerland, 2018.
44. Kruger, J.; Plessis, A.D.; van Zijl, G. An investigation into the porosity of extrusion-based 3D printed concrete. *Addit. Manuf.* **2021**, *37*, 101740. [CrossRef]
45. Van Der Putten, J.; Deprez, M.; Cnudde, V.; De Schutter, G.; Van Tittelboom, K. Microstructural Characterization of 3D Printed Cementitious Materials. *Materials* **2019**, *12*, 2993. [CrossRef] [PubMed]
46. Zhou, Y.; Gencturk, B.; Willam, K.; Attar, A. Carbonation-Induced and Chloride-Induced Corrosion in Reinforced Concrete Structures. *J. Mater. Civ. Eng.* **2015**, *27*, 04014245. [CrossRef]

Disclaimer/Publisher's Note: The statements, opinions and data contained in all publications are solely those of the individual author(s) and contributor(s) and not of MDPI and/or the editor(s). MDPI and/or the editor(s) disclaim responsibility for any injury to people or property resulting from any ideas, methods, instructions or products referred to in the content.